Organic Field-Effect Transistors Utilizing Solution-Deposited Oligothiophene-Based Swivel Cruciforms

Achmad Zen,[†] Patrick Pingel,[†] Frank Jaiser,[†] Dieter Neher,*[,†] Jörg Grenzer,[‡] Wei Zhuang,[⊥] Jürgen P. Rabe,[⊥] Askin Bilge,[||] Frank Galbrecht,[||] Benjamin S. Nehls,[||] Tony Farrell,*[,||] Ullrich Scherf,*[,||] Ruben D. Abellon,[§] Ferdinand C. Grozema,[§] and Laurens D. A. Siebbeles[§]

Institute of Physics, University of Potsdam, Am Neuen Palais 10, D-14469 Potsdam, Germany, Institute of Ion Beam Physics and Materials Research, Bautzner Landstrasse 128, D-01328 Dresden, Germany, Department of Physics, Humboldt University Berlin, Newtonstrasse 15, D-12489 Berlin, Germany, Macromolecular Chemistry, University of Wuppertal, Gauss-Strasse 20, D-42097 Wuppertal, Germany, and Interfaculty Reactor Institute, Delft University of Technology, Mekelweg 15, 2629 JB Delft, The Netherlands

Received August 24, 2006. Revised Manuscript Received January 9, 2007

Two types of highly soluble oligothiophene-based swivel cruciforms are presented as semiconducting materials in OFETs. Incorporation of these penta-aryl oligomers into a swivel-cruciform type architecture greatly enhances the solubility of the oligomers, which lends itself to the fluidic preparation of thin films of the materials. XRD and AFM analysis of the resulting thin films reveals that they are highly crystalline. OFETs with pentathiophene-based swivel cruciforms exhibit a maximum field-effect mobility of 0.012 cm^2/Vs, which is among the highest values reported to date for wet-processed OFETs utilizing oligothiophenes. In contrast, transistors made from bithiophene-phenyl-based cruciforms give overall lower mobilities, although the layers appear more crystalline in the AFM images. Pulse-radiolysis time-resolved microwave conductivity (PR-TRMC) experiments of the swivel cruciforms suggest that charge transport between crystalline domains may ultimately be the determining factor.

1. Introduction

In the areas of organic field-effect transistors (OFETs) and photovoltaic devices, the challenge is to generate supramolecular organization in order to maximize the necessary long-distance directional energy and electron transfer. There are two main routes to constructing organic-based thin film transistors, namely via the polymeric and small molecule approaches. Equally important to the progress of organic electronics is the development of innovative, inexpensive processing techniques allowing the fabrication of low-cost devices.[1] These can be grouped into two main categories: "wet", solution-based methods and "dry" processes such as vapor-phase deposition. The prospect of processing π-conjugated materials from solution, thereby lending themselves to techniques such as ink-jet printing, has enormous appeal to researchers working in the area of organic-based electronic devices.[2]

Although thin films fabricated from π-conjugated polymers such as poly(3-hexylthiophene) (P3HT) can be easily processed from solution, their charge-carrier mobilities are highly influenced by the purity,[3] regioregularity,[4] and molecular weight[5] of the P3HT. Mobilities of up to 0.1 cm^2/Vs at room temperature are observed for high regioregularity P3HT using optimized processing conditions. Such samples exhibit a microphase-separated morphology with layers of regularly packed main chains separated by the disordered side chains. Note that very recently, McCulloch et al. reported on layers of liquid-crystalline poly(2,5-bis(3-alkylthiophen-2-yl)thieno-[3,2-b]thiophene), which exhibit a highly organized morphology after processing in the mesophase. Using this approach, high charge-carrier mobilities of up to 0.7 cm^2/Vs could be achieved.[6]

Small molecules have also been widely studied because of their relatively facile purification and well-defined chemical structure. Oligothiophenes in particular have been extensively investigated as components in OFETs and exhibit

* To whom correspondence should be addressed. E-mail: neher@uni-potsdam.de (D.N.); scherf@uni-wuppertal.de (U.S.); tony.farrell@ge.com (T.F.).
[†] University of Potsdam.
[‡] Institute of Ion Beam Physics and Materials Research.
[⊥] Humboldt University Berlin.
[||] University of Wuppertal.
[§] Delft University of Technology.

(1) Forrest, S. R. *Nature* **2004**, *428*, 911.
(2) (a) Bao, Z.; Rogers, J. A.; Katz, H. E. *J. Mater. Chem.* **1999**, *9*, 1895. (b) Sirringhaus, H. *Adv. Mater.* **2005**, *17*, 2411.
(3) Dicker, G.; de Haas, M. P.; Warman, J. M.; de Leeuw, D. M.; Siebbeles, L. D. A. *J. Phys. Chem. B* **2004**, *108*, 17818.
(4) (a) Bao, Z.; Dodabalapur, A.; Lovinger, A. J. *Appl. Phys. Lett.* **1996**, *69*, 4108. (b) Sirringhaus, H.; Brown, P. J.; Friend, R. H.; Nielsen, M. M.; Bechgaard, K.; Langeveld-Voss, B. M. W.; Spiering, A. J. H.; Janssen, R. A. J.; Meijer, E. W.; Herwig, P. T.; de Leeuw, D. M. *Nature* **1999**, *685*, 857.
(5) (a) Kline, R. J.; McGehee, M. D.; Kadnikova, E. N.; Liu, J.; Frechet, J. M. J. *Adv. Mater.* **2003**, *15*, 1519. (b) Kline, R. J.; McGehee, M. D.; Toney, M. F. *Nature Mater.* **2006**, *5*, 222. (c) Kline, R. J.; McGehee, M. D.; Kadnikova, E. N.; Liu, J.; Frechet, J. M. J.; Toney, M. F. *Macromolecules* **2005**, *38*, 3312. (d) Zen, A.; Pflaum, J.; Hirschmann, S.; Zhuang, W.; Jaiser, F.; Asawapirom, U.; Rabe, J. P.; Scherf, U.; Neher, D. *Adv. Funct. Mater.* **2004**, *14*, 757. (e) Zen, A.; Saphiannikova, M.; Neher, D.; Grenzer, J.; Grigorian, S.; Pietsch, U.; Asawapirom, U.; Janietz, S.; Scherf, U.; Lieberwirth, I.; Wegner, G. *Macromolecules* **2006**, *39*, 2162.
(6) McCulloch, I.; Heeney, M.; Bailey, C.; Genevicius, K.; Macdonald, I.; Shkunov, M.; Sparrowe, D.; Tierney, S.; Wagner, R.; Zhang, W.; Chabinyc, M. L.; Kline, R. J.; McGehee, M. D.; Toney, M. F. *Nat. Mater.* **2006**, *5*, 328.

10.1021/cm062000p CCC: $37.00
Published on Web 02/23/2007

reasonable mobilities when deposited by thermal evaporation in vacuum (<1 cm^2/Vs).[7] Vacuum deposition techniques generally produce better-ordered layers with higher magnitude mobilities than those prepared from solution (<0.1 cm^2/Vs).[8] However, these processes can be costly and tend to be wasteful of material. On the other hand, the possibility of using liquid-phase techniques is viewed as a low-cost alternative and concomitantly crucial if organic transistors are to be implemented in large-area electronic substrates in a cost-appealing manner.

Many design strategies have been investigated in an attempt to achieve self-assembly of π-conjugated systems.[9] One of the most important secondary interactions that results in supramolecular order is $\pi-\pi$ interactions. We recently reported on an interesting architecture, the swivel cruciform, that exhibits strong $\pi-\pi$ intramolecular interactions, even in solution.[10] We adapted this molecular design to produce a novel $\pi-\pi$ -dihexylpentathiophene based swivel-cruciform that exhibit a field-effect mobility of 0.012 cm^2/Vs. This is one of the highest FET mobilities fabricated from solution-processed oligothiophenes.[2b] Herein, we report on the synthesis of another thienyl-based swivel-cruciform and provide detailed investigations of the thermal, structural, and electronic properties of both penta-aryl cruciform dimers.

2. Results and Discussion

The synthesis of DHPT-SC has been previously reported, and the strategy is illustrated in Scheme 1.[11] For the synthesis of the (dihexyl-bithiophene)$_2$-phenyl swivel cruciform (DHBTP-SC), we returned to the route devised for the preparation of the analogous all-phenylene cruciforms.[12] The very different reactivity of the bromo and chloro groups under Suzuki-type aryl−aryl coupling gave HTP in reasonable yield. A subsequent nickel-mediated coupling of HTP via the so-called Yamamoto procedure under microwave heating[12] gave a pure sample of the swivel-cruciform DHBTP-SC in 25% yield (Scheme 2). Once again the solubility of the cruciform in organic solvents was much better than the cruciform "arm" and allowed for the full characterization of the new compound by NMR spectroscopy (see the Supporting Information).

Scheme 1. Synthesis of DHPT-SC[a]

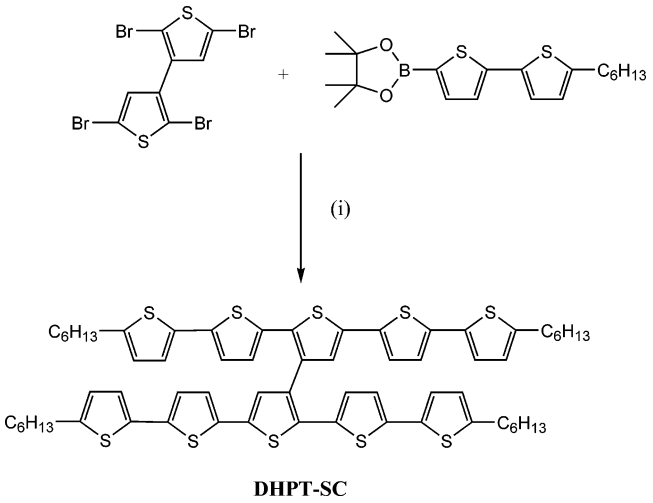

DHPT-SC

[a] (*i*) $Pd[P(Ph)_3]_2Cl_2$, KOH, THF, reflux, 24 h.

We have previously noted that materials based on a swivel cruciform motif exhibit a propensity toward intramolecular $\pi-\pi$ interaction in solution as well as in the solid state.[10−12] The folded structure of DHBTP-SC in solution is clearly established by comparing the ^1H NMR of the swivel cruciform with that of the precursor arm HTP. Analysis of the correlated NMR spectra (see the Supporting Information) allows a full assignment of the signals; the labeling scheme is illustrated in Scheme 2. Noteworthy is that there is not a significant shift in the signals arising from the three central phenyl protons or from the terminal thienyl proton signals labeled *i* and *k*. However, when comparing ^1H NMR spectra of the precursor HTP and the swivel cruciform DHBT-SC, we observe a dramatic change in the ^1H chemical shifts of the four protons associated with the thienyl units directly attached to the phenyl moiety (see the Supporting Information, Figure S1). For example, in the case of HTP, all four signals are found between 7.0 and 7.3 ppm, whereas in the ^1H NMR spectrum of DHBTP-SC, three of these signals are observed between 6.4 and 6.8 ppm. This is consistent with our previous findings for cruciforms comprised of three and five aryl units in that molecules based on this type of architecture adopt a folded structure as depicted in Scheme 2, even in solution.[10] We propose that this is driven by strong intramolecular $\pi-\pi$ interaction between the thienyl units in the ortho-positions of the central biphenyl bridging unit of the cruciform. In fact, the introduction of a central biphenyl core in DHBTP-SC should lead to an increased distortion within the individual bis(dithienyl)penylene arms and to a somewhat reduced intermolecular interaction in the solid state. This may be documented in the observed lower hole mobility. On the other side, the increased HOMO−LUMO

(7) (a) Halik, M.; Klauk, H.; Zschieschang, U.; Schmid, G.; Ponomarenko, S.; Kirchmeyer, S.; Weber, W. *Adv. Mater.* **2003**, *15*, 917. (b) Crouch, D. J.; Skabara, P. J.; Heeney, M.; McCulloch, I.; Coles, S. J.; Hursthouse, M. B. *Chem. Commun.* **2005**, *11*, 1465. (c) Yoon, M. H.; DiBenedetto, S. A.; Facchetti, A.; Marks, T. J. *J. Am. Chem. Soc.* **2005**, *127*, 1348. (d) Facchetti, A.; Mushrush, M.; Katz, H. E.; Marks, T. J. *Adv. Mater.* **2003**, *15*, 33. (e) Tian, H.; Wang, J.; Shi, J.; Yan, D.; Wang, L.; Geng, Y.; Wang, F. *J. Mater. Chem.* **2005**, *15*, 3026. (f) Facchetti, A.; Letizia, J.; Yoon, M. H.; Mushrush, M.; Katz, H. E.; Marks, T. J. *Chem. Mater.* **2004**, *16*, 4715. (g) Tian, H.; Shi, J.; Yan, D.; Wang, L.; Geng, Y.; Wang, F. *Adv. Mater.* **2006**, *18*, 2149.

(8) (a) Laquindanum, J. G.; Katz, H. E.; Lovinger, A. J. *J. Am. Chem. Soc.* **1998**, *120*, 664. (b) Katz, H. E.; Laquindanum, J. G.; Lovinger, A. J. *Chem. Mater.* **1998**, *10*, 633. (c) Ponomarenko, S.; Kirchmeyer, S.; Elschner, A.; Huisman, B. H.; Karbach, A.; Dreschler, D. *Adv. Funct. Mater.* **2003**, *13*, 591. (d) Mushrush, M.; Facchetti, A.; Lefenfeld, M.; Katz, H. E.; Marks, T. J. *J. Am. Chem. Soc.* **2003**, *125*, 9414. (e) Chang, P. C.; Lee, J.; Huang, D.; Subramanian, V.; Murphy, A. R.; Frechet, J. M. J. *Chem. Mater.* **2004**, *16*, 4783.

(9) Hoeben, F. J. M.; Jonkheijm, P.; Meijer, E. W.; Schenning, A. P. H. J. *Chem. Rev.* **2005**, *105*, 1491.

(10) (a) Nehls, B. S.; Galbrecht, F.; Bilge, A.; Brauer, D. J.; Lehmann, C. W.; Scherf, U.; Farrell, T. *Org. Biomol. Chem.* **2005**, *3*, 3213.(b) Nehls, B. S.; Galbrecht, F.; Bilge, A.; Scherf, U.; Farrell, T. *Macromol. Symp.* **2006**, *239*, 21. (c) Bilge, A.; Zen, A.; Forster, M.; Li, H.; Galbercht, F.; Nehls, B.; Farrell, T.; Neher, D.; Scherf, U. *J. Mater. Chem.* **2006**, *16*, 3177.

(11) Zen, A.; Bilge, A.; Galbrecht, F.; Alle, R.; Meerholz, K.; Grenzer, J.; Neher, D.; Scherf, U.; Farrell, T. *J. Am. Chem. Soc.* **2006**, *128*, 3914.

(12) (a) Carter, K. R. *Macromolecules* **2005**, *35*, 6757. (b) Galbrecht, F.; Yang, X. H.; Nehls, B. S.; Neher, D.; Farrell, T.; Scherf, U. *Chem. Commun.* **2005**, *18*, 2378. (c) Nehls, B. S.; Asawapirom, U.; Fuldner, S.; Preis, E.; Farrell, T.; Scherf, U. *Adv. Funct. Mater.* **2004**, *14*, 352.

Scheme 2. Synthesis of DHBTP-SC[a]

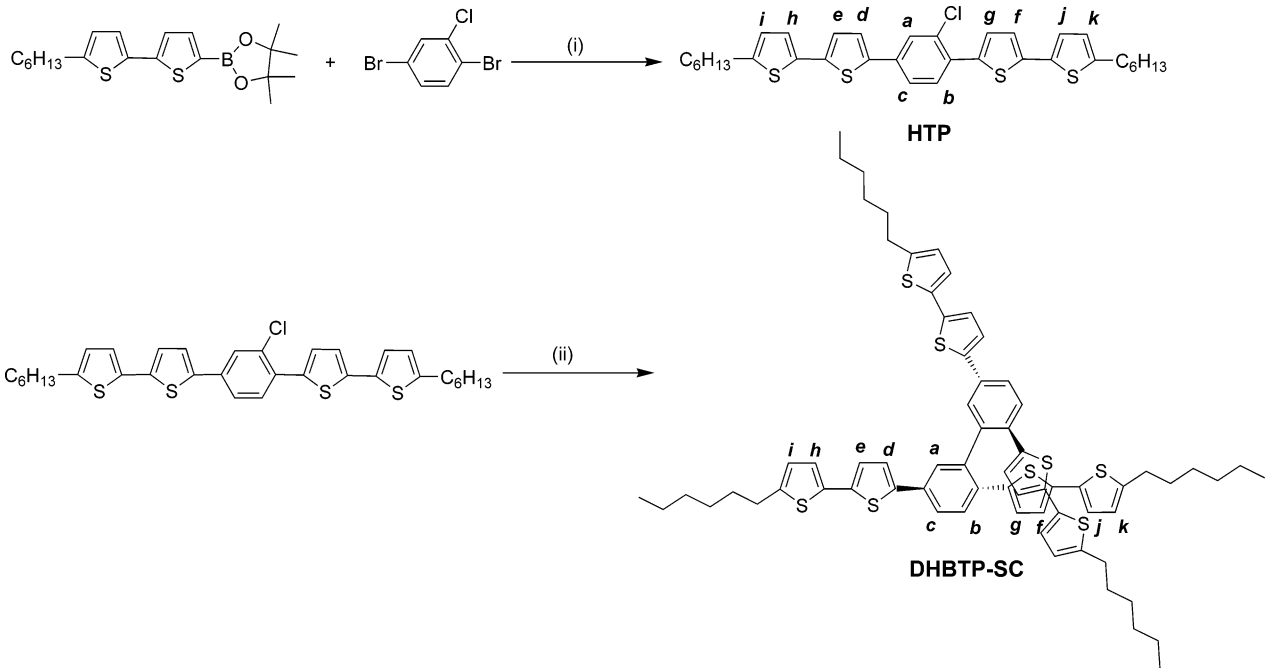

[a] (*i*) $Pd[P(Ph)_3]_2Cl_2$, KOH, THF, reflux, 24 h; (ii) $Ni(COD)_2$, COD, and 2,2′-bipyridine in toluene/DMF, reflux, 3 days.

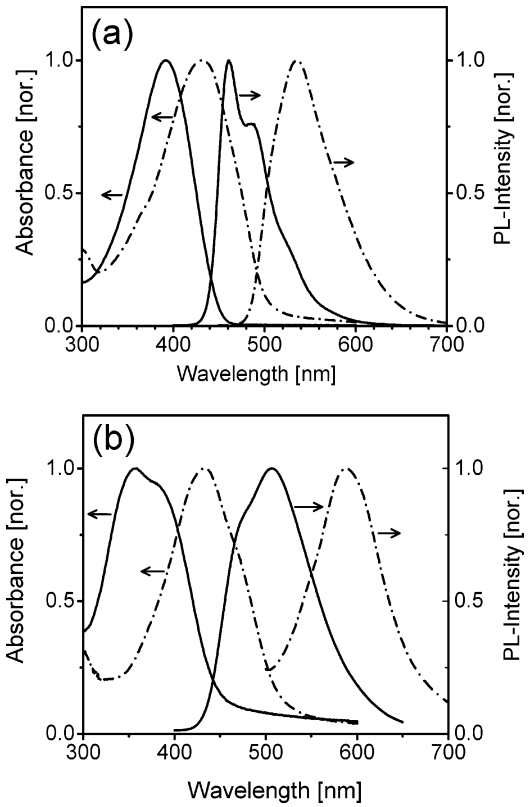

Figure 1. Absorption and photoluminescence spectra of DHBTP-SC (solid lines) and DHPT-SC (dashed-dotted lines) in (a) chloroform solution and (b) thin films.

energy gap of DHBTP-SC should make the dimer more stable to oxidative degradation.

Optical Properties. The optical absorption and emission spectra of dilute chloroform solutions of DHBTP-SC and DHPT-SC are shown in Figure 1a. The absorption spectra for both oligomers are broad and featureless with the all-thiophene cruciform DHPT-SC exhibiting the lower-energy absorption, as expected. Unlike the broad emission peak of DHPT-SC in solution (536 nm), the emission spectrum of DHBTP-SC exhibits two well-resolved maxima located at 461 and 484 nm. This may indicate that the emitting species adopts a more planar ordered structure in solution upon photoexcitation. Comparing the spectra recorded in solution and thin films, the cruciforms exhibit no strong changes in absorption (Figure 1b). This may indicate that the ground state conformation is quite similar. The energy band gap (E_g), calculated from the onset of the solid-state absorption spectra, taking into account an exciton energy binding of 300 meV, yields values of $E_g = 3.05$ and 2.65 eV for DHBTP-SC and DHPT-SC, respectively. For both cruciforms, the solid-state emission spectra exhibit a significant red shift and become broader compared to their spectra recorded in solution. This is a common feature of the optical spectra of swivel cruciform structures, and it is postulated that this is due to the formation of an intramolecular excimer upon photoexcitation.

Thermal Properties. The thermal properties of the oligomers were measured by differential scanning calorimetry (DSC), and the curves from the second heating/cooling cycle are shown in Figure 2. Both oligomers exhibit good thermal stability with melting and crystallization temperatures above 150 °C, whereas the sharpness of melting and crystallization peaks indicate good ordering within the materials. The endothermic melting enthalpies for DHBTP-SC and DHPT-SC were calculated from the integration of the melting curves and are 55.93 and 50.90 J/g, respectively. They are ca. three times higher than the melting enthalpy measured for the highest molecular weight of P3HT.[5e] The complete data determined from the DSC runs on the powder samples are listed in Table 1.

Morphology. *XRD Studies.* Figure 3a shows the reflectivity and XRD-GID (grazing incidence angle XRD) measured for thin films (40−55 nm) of DHBTP-SC. The films

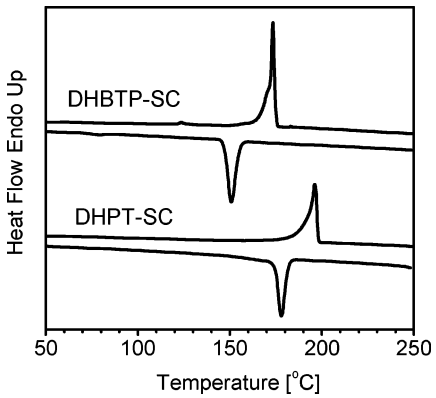

Figure 2. DSC thermograms of powder samples measured from DHBTP-SC and DHPT-SC.

Table 1. Melting Temperature (T_m), Crystallization Temperature (T_c), and Melting Enthalpies (ΔH_m) Measured from Powder Samples Using DSC

oligomer	T_m (°C)	T_c (°C)	ΔH_m (J/g)
DHBTP-SC	173.5	150.8	55.93
DHPT-SC	196.2	177.9	50.90

were prepared from chloroform solutions and subsequently annealed at 120 °C for 5 min followed by slow cooling at a rate of 1.3 K/min. The first- and second-order Bragg peaks are clearly resolved in the reflectivity measurement, as shown in the top curve (black line). The *d*-spacing calculated from the reflectivity curve is 3.2 nm and attributed to the intermolecular distance between two neighboring molecules of DHBTP-SC within the lamellar structure. From the full width at half-maximum (FWHM) of the Bragg peaks, the average domain size was estimated to be 30 nm. However, the FWHM increases with the Bragg peak order, indicating a fluctuation of the intermolecular distance of roughly 4%. Further XRD-GID measurements were performed to investigate the surface and bulk crystallinity. Thin films from DHBTP-SC displayed first- and second-order Bragg peaks that are independent in intensity of the incidence angles, indicating that the thin films of DHBTP-SC are uniformly crystalline throughout the layers (Figure 3a, colored curves). Figure 3b shows the reciprocal space map at small incidence angles (denoted here as incidence angle). In this figure, the intensity distribution of the first- and second-order Bragg peaks can be clearly identified (see the horizontal stripes). With increasing incidence angles, the intensity patterns at the first- and second-order Bragg peaks are homogeneous, which indicates that the crystalline domains are almost without any preferential orientation throughout the layer.

Figure 3c shows the reflectivity (black curve) and XRD-GID data (colored curves) obtained from thin films comprised of DHPT-SC. In the reflectivity curve, Kiessig peaks can be observed at low angles, indicating that the DHPT-SC forms very smooth layers. From the distance between two Kiessig peaks, one obtains an overall layer thickness of 52 nm. The *d*-spacing for the intermolecular distance between two neighboring molecules of DHPT-SC within the lamellar structure is 3 nm, as calculated from the first- and second-order Bragg peaks. This value is slightly smaller than that found in the films of DHBTP-SC but larger than the values for the related linear oligomers such as α,ω-dihexylquaterthiophene[13] or α-quinquethiophene.[14] From the FWHM of these peaks, we calculated the domain size in these films to be about 25 nm. The XRD-GID shows that the Bragg peaks are only discernible when the X-ray wave penetrates deep into the film; that is, when the incidence angles α_i is larger than the critical angle of the total external refraction α_c. This clearly indicates that thin films from DHPT-SC are less crystalline in the surface compared to the bulk. Figure 3d shows the reciprocal space map at small incidence angles for DHPT-SC. Here, it is observed that upon increasing the incidence angle, the intensity patterns from the first- and second-order Bragg peaks are not homogeneous. Instead, they become more intense with increasing incidence angles, which confirms that the crystalline domains are mainly in the bulk. Moreover, the FWHM of the first-order Bragg peak decreases slightly with increasing incidence angle, indicating that the domain size at the sample surface is much smaller (ca. 10 nm) compared to the domain size in the bulk (ca. 25 nm).

AFM Studies. We investigated the effect of annealing on the crystallinity of the oligomers by heating thin films (the same samples as investigated in OFETs) of both cruciforms at 120 °C for 30, 90, and 120 min and compared them to the AFM images of the as-prepared samples. Figure S2 of the Supporting Information displays the height and phase images from thin films of cruciform DHBTP-SC as-prepared (see the Supporting Information, parts a and b of Figure S2) and after annealing at 120 °C for different time periods (see the Supporting Information, Figure S2c−h). It can be clearly seen that the size of grains, which we attribute to crystalline domains, as evidenced by the X-ray data, increases clearly with annealing time. To quantify the growth, we calculated the root-mean-square roughness (R_{RMS}) using the equation

$$R_{RMS} = \sqrt{\frac{\sum_{i=1}^{N} (Z_i - Z_{avg})^2}{N}} \quad (1)$$

and the mean roughness R_a

$$R_a = \frac{\sum_{i=1}^{N} |Z_i - Z_{CP}|}{N} \quad (2)$$

wherein Z_i is the current height of the thin films measured perpendicular to the substrate (Z value), Z_{avg} is the average Z values within the given area, N is the number of points within the given area, and Z_{CP} is the Z value at the center plane.

The R_{RMS} and R_a values calculated for both swivel cruciforms as-prepared and after annealing at 120 °C for various periods of time are presented in Table 2. For DHBTP-SC, the data illustrate that annealing the layer for 30 min already leads to a significant roughening of the surface from 1.1 nm for the as-prepared sample to 6.8 nm.

(13) Moret, M.; Campione, M.; Borghesi, A.; Miozzo, L.; Sassella, A.; Trabattoni, S.; Lotz, B.; Thierry, A. *J. Mater. Chem.* **2005**, *15*, 2444.
(14) Melucci, M.; Gazzano, M.; Barbarella, G.; Cavallini, M.; Biscarini, F.; Maccagnani, P.; Ostoja, P. *J. Am. Chem. Soc.* **2003**, *125*, 10266.

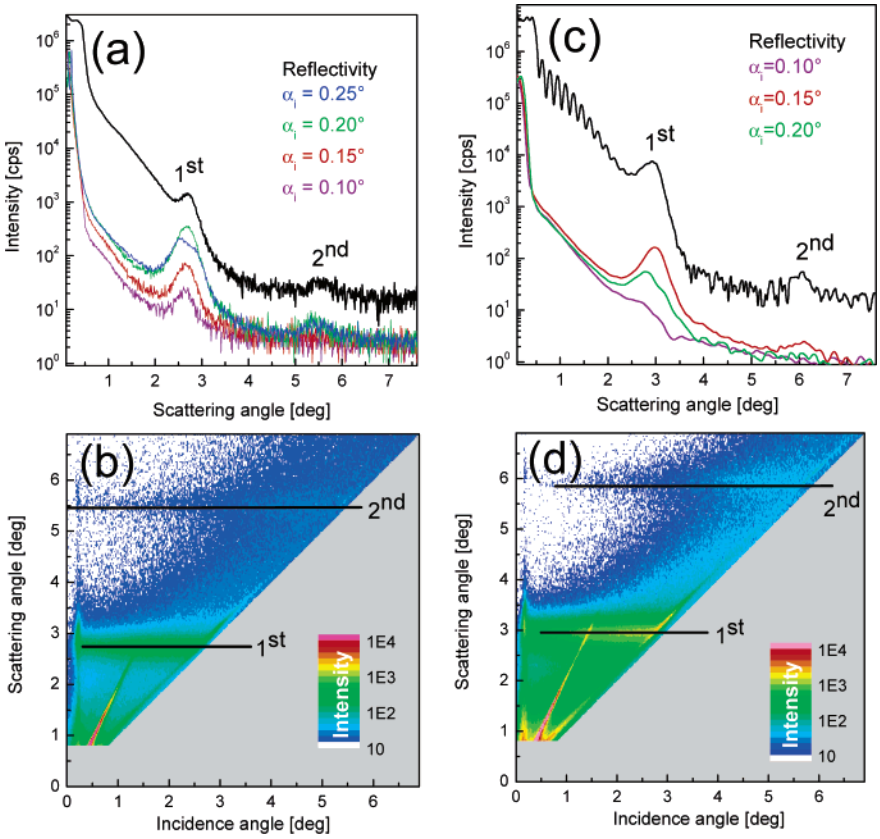

Figure 3. XRD images of DHBTP-SC and DHPT-SC that have been annealed at 120 °C for 5 min inside a N_2-filled glove box, followed by slow cooling to room temperature with a cooling rate of 1.3 K/min. (a) Reflectivity measurement (black line) and powder scans of DHBTP-SC with different angle of incidence (colored). (b) Reciprocal space map at small angles from powder scans of DHBTP-SC; the Bragg peaks can be clearly observed (horizontal stripes); the intensity at first and second-order Bragg peaks are homogeneous with increasing incidence angle. (c) Reflectivity measurement (black line) and powder scans of DHPT-SC with different angle of incidence (colored). (d) Reciprocal space map at small angles from powder scans of DHPT-SC; the first and second order of the Bragg peaks can be clearly observed (horizontal stripes) and become highly intense with increasing incidence angle.

Table 2. Root-Mean-Square Roughness (R_{RMS}) and the Mean Roughness (R_a) for Both Swivel Cruciforms Calculated Using Veeco Software and Using AFM Pictures Shown in Figures S2a−h and S3a−h

treatments	DHBTP-SC R_{RMS} (nm)	DHBTP-SC R_a (nm)	DHPT-SC R_{RMS} (nm)	DHPT-SC R_a (nm)
as-prepared	1.4	1.1	2.3	1.8
annealed at 120 °C, 30 min	10.1	6.8	2.1	1.7
annealed at 120 °C, 90 min	10.6	7.4	2.3	1.8
annealed at 120 °C, 120 min	12.7	9.6	4.5	3.4

It is attributed to the growth of large crystallites that protrude from the surface. After 120 min annealing, R_a increases further to 9.6 nm. Note that the reciprocal space map as shown in Figure 3b revealed that thin films from DHBTP-SC are crystalline throughout the whole layer after annealing. Apparently, the crystallites seen at the surface extend deep into the thin films and probably down to the substrate.

On the other hand, DHPT-SC shows a rather different behavior under the same conditions. If we compare the AFM images of the as-prepared sample (see the Supporting Information, parts a and b of Figure S3) to annealed samples (see the Supporting Information, Figure S3c−h), it is difficult to observe any significant differences in the morphologies. This is in agreement with the results from the X-ray measurements, which suggested that a short time of annealing does not initiate the growth of large crystallites at the surface of DHPT-SC. Nonetheless, the reciprocal space map in Figure 3d clearly shows that the layer is highly crystalline in the bulk. However, when the samples were annealed at 120 °C for 120 min, a significant increase in the R_{RMS} and R_a values was observed. In fact, these AFM studies also suggest that the change in surface morphology as indicated by the increase in R_{RMS} and R_a values upon annealing is a nonlinear process for both cruciforms (see Table 2).

OFET Studies. The output characteristics of transistors based on both oligomers (as-prepared and annealed) show well-resolved linear and saturation regions (panels a and b of Figure 4). The absence of hysteresis during the measurement cycles indicates good stability and high purity of the materials. The current on/off ratio, which is the ratio of maximum drain current (the "on" current of the OFET) to the minimum drain current (the "off" current of the OFET), is $>1 \times 10^4$ for both oligomers. A large on/off current ratio is essential, because most electronic applications require the transistor to behave as a switch, with a large drain current in the "on" state, and a negligible drain current in the "off" state.[15] Figure 5 shows the plot of the square root of the drain current in the saturation region $I_{DS,sat}^{1/2}$ vs the gate

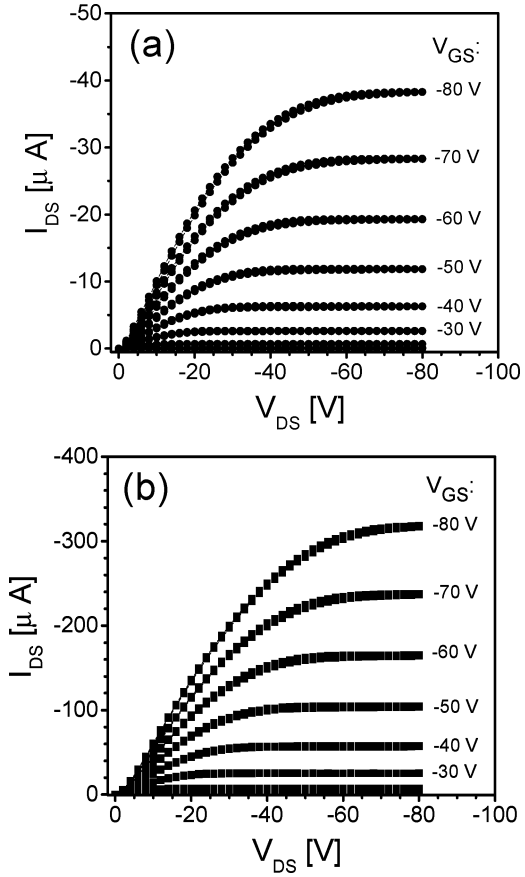

Figure 4. Output characteristics of OFET devices measured from as-prepared sample of (a) DHBTP-SC and (b) DHPT-SC.

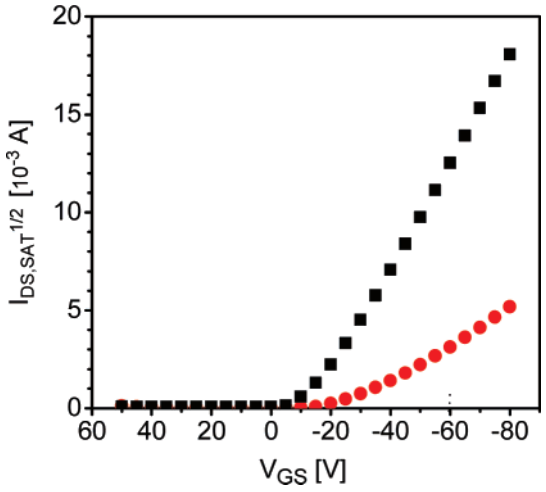

Figure 5. Square-root plot of $I_{DS,Sat}^{1/2}$ vs V_{GS} from OFET devices shown in Figure 6 with DHBTP-SC (●) and DHPT-SC (■) as the semiconductors.

voltage V_{GS} from which the field-effect mobilities at saturation region were calculated using the following relation

$$\sqrt{I_{DS,sat}} = \sqrt{\frac{WC_i}{2L}\mu_{sat}}\,(V_{GS} - V_{th}) \qquad (3)$$

Here, W and L are the channel width and length, respectively, and C_i is the capacitance per unit area of the SiO_2 insulator, whereas μ_{sat} is the field-effect mobility in the saturation region and V_{th} is the threshold voltage of the transistor. For transistors with as-prepared thin films made from DHBTP-SC, we measured a field-effect mobility of ca. 0.001 cm^2/Vs. With the same treatment, transistors from DHPT-SC exhibited a field-effect mobility of ca. 0.01 cm^2/Vs. Note that the field-effect mobilities varied by ca. 20% when comparing different sets of transistors.[16] These mobilities are among the best for solution-processed oligomers at room temperature but smaller than mobilities measured in substituted acenes[15] and solution-processing α,ω-substituted sexithiophene derivatives containing thermally removable solubilizing groups.[17]

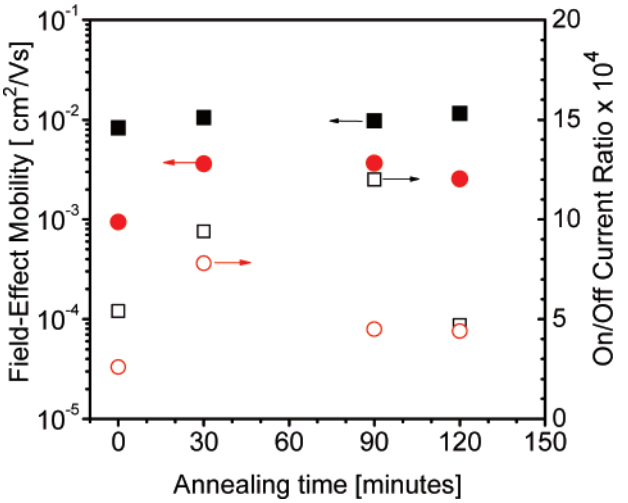

Figure 6. Field-effect mobilities and current on/off ratios of OFET devices annealed at 120 °C for different time intervals, using DHBTP-SC (circle) and DHPT-SC (rectangle) as the semiconductors. Open symbols depict the on/off current ratio, whereas solid symbols for a field-effect mobility.

Our previous studies using P3HT revealed that thermal treatment of the thin films prior to the deposition of source-drain electrodes improves the OFET performance.[5d,16] For these oligomers, we found that annealing the thin films of both oligomers at 120 °C gave the best optimum OFET performance. This is not surprising, as it is well-known that the annealing process affects the morphology of organic materials.[5d,18] Further, studies on P3HT with different molecular weights indicated that there exists a direct correlation between the crystallinity and the field-effect mobility.[5e] Hence, we compared the OFET performances of the as-prepared layers to thin films that were annealed at 120 °C for 30, 90, and 120 min prior to deposition of the Au source and drain electrodes (Figure 6). Interestingly, there is a 4-fold increase in the mobilities of the OFETs prepared from DHBTP-SC layers after 30 min annealing. This might be explained by the significant change in the morphologies after the first annealing step (see the Supporting Information, Figure S2a−h). However, prolonged annealing does not increase the mobilities further. This indicates that the overall

(15) Gamota, D. R.; Brazis, P.; Kalyanasundaram, K.; Zhang, J., Eds. *Printed Organic and Molecular Electronics*; Kluwer Academic Publisher: Dordrecht, The Netherlands, 2004.

(16) (a) Zen, A.; Neher, D.; Silmy, K.; Hollander, A.; Asawapirom, U.; Scherf, U. *Jpn. J. Appl. Phys., Part 1* **2005**, *44*, 3721. (b) Zen, A.; Saphiannikova, M.; Neher, D.; Asawapirom, U.; Scherf, U. *Chem. Mater.* **2005**, *17*, 781.

(17) Chang, P. C.; Lee, J.; Huang, D.; Subramanian, V.; Murphy, A. R.; Frechet, J. M. J. *Chem. Mater.* **2004**, *16*, 4783.

(18) (a) Sperling, L. H., Ed. *Introduction to Physical Polymer Science*; John Wiley & Sons: New York, 2001. (b) Reiter, G., Sommer, J. U., Eds. *Polymer Crystallization*; Springer: Berlin, 2003.

size of the crystals does not have a major impact on the transport properties. On the other hand, there is no significant change in the OFET mobilities prepared from the as-prepared or the annealed films of DHPT-SC, even after 120 min of annealing. For all preparation conditions, the on/off current ratio (Figure 6) remains quite high, indicating the overall good quality of all transistors.

Temperature Dependence of OFET Mobility. The temperature dependence of the mobilities in OFETs prepared from both cruciforms is shown in panels a and b of Figure 7, respectively. The OFET measurements were recorded in situ upon heating and subsequently upon cooling. In both cases, the mobility follows a typical Arrhenius temperature dependence of the form

$$\mu(T) = \mu_0 \exp\left(-\frac{E_a}{kT}\right) \quad (4)$$

where $\mu(T)$ is the temperature-activated mobility, μ_0 is the prefactor, E_a is the activation energy, k is the Boltzmann constant, and T is the absolute temperature. For both oligomers, the activation energies are slightly smaller when recorded upon cooling. It has been suggested that thermal treatment to organic thin films leads to reduction of free volume in the layer and removal of residual solvent, thus leading to more compact and ordered films.[19] In the case of DHBTP-SC, the E_a upon heating is 80 meV compared to E_a = 51 meV upon cooling (Figure 7a). Note that the samples were kept for 10 min at 120 °C before the cooling measurement started, during which time significant changes in the morphologies of the thin films might have occurred, as described above. Therefore, the resulting curve is shifted compared to the heating run. For OFETs prepared from DHPT-SC (Figure 7b), the activation energies are 88 and 52 meV upon heating and cooling, respectively. Within the experimental uncertainties, these values compare well with those measured for DHBTP-SC.

Influence of Traps and Temperature Dependence of Mobilities. Pulse-radiolysis time-resolved microwave conductivity (PR-TRMC) measurements were performed for both cruciforms in order to obtain the charge-carrier mobility at a probing frequency close to 30 GHz using irradiation pulses of 10 ns. There is an important difference in the distance scale on which the charge transport is probed in TRMC and in OFET measurements. In OFET, charge carriers have to move through the entire sample from the source to the drain electrodes in order to contribute to the conductivity. In TRMC experiments, the charge transport is probed on a local scale and it is the charges that move back and forth inside a single grain of the material that contribute to the conductivity. Therefore, TRMC mobilities are generally expected to be higher than OFET mobilities, because in the former, the mobility is not limited by the charge transport across grain boundaries. Comparison of mobilities measured with PR-TRMC and in the OFET might thus provide valuable information on carrier trapping at grain boundaries in the device.

(19) Abdou, M. S. A.; Lu, X.; Xie, Z. W.; Orfino, F. P.; Deen, M. J.; Holdcroft, S. *Chem. Mater.* **1995**, *7*, 631.

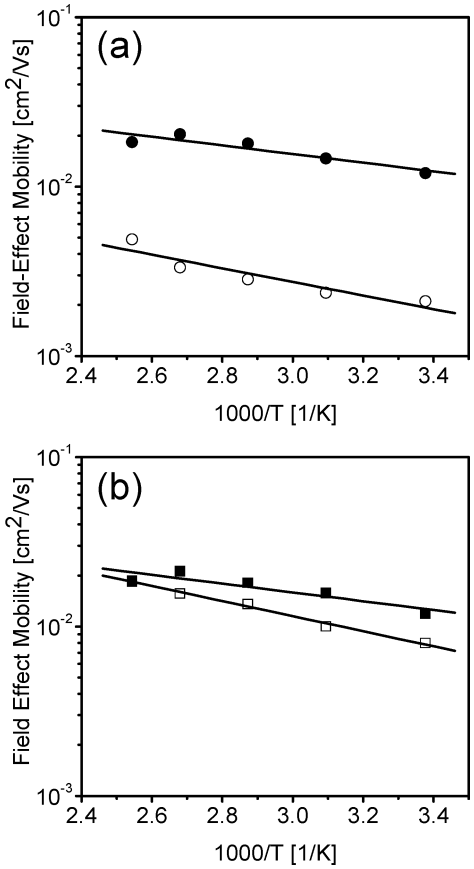

Figure 7. Temperature dependence of charge-carrier mobilities extracted from OFET measurements using DHBTP-SC (circles) and DHPT-SC (rectangle). Open symbols depict data measured with increasing temperatures and solid symbols depcit those measured for decreasing temperatures. Note that the samples were kept for 10 min at 120 °C before the cooling cycle started.

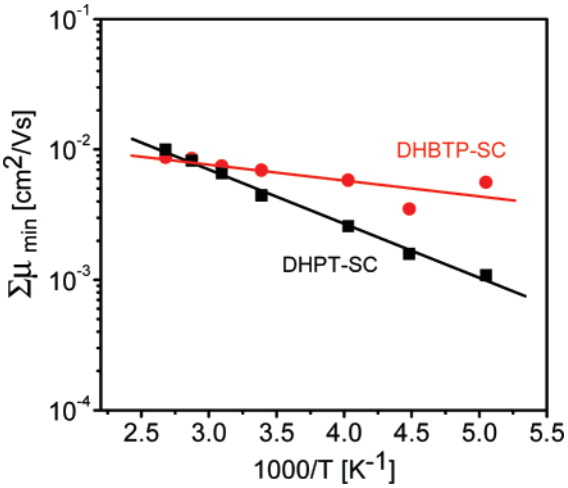

Figure 8. Temperature dependence of the charge-carrier mobilities extracted from PR-TRMC measurements using DHBTP-SC (●) and DHPT-SC (■) powders.

The mobilities derived from the radiation-induced conductivity measurements are shown as a function of temperature in Figure 8. At room temperature, the TRMC mobility in DHBTP-SC (6.9×10^{-3} cm^2/Vs) is somewhat higher than that for DHPT-SC (4.5×10^{-3} cm^2/Vs), in contrast to the OFET measurements, where it was found that the mobility

for DHPT-SC is generally higher. On the other hand, the overall values determined with PR-TRMC are slightly smaller than those measured in the OFET geometry upon cooling. It should be noted that the mobilities shown in Figure 8 are the minimum values, assuming that all the charge that is initially generated survives until after the pulse. Because charges may decay by recombination and trapping already during the irradiation pulse, the actual microwave mobility is expected to be significantly higher. Because of this complication, it is difficult to compare the microwave mobility values and the data obtained from OFET measurements quantitatively.

As shown in Figure 8, there are significant differences in the temperature-dependent mobilities obtained for the swivel cruciforms. First, the temperature dependence of DHBTP-SC is not as steep as that for DHPT-SC. For DHBTP-SC, the activation energy is only 25 meV, which is significantly smaller than the value determined from the temperature-dependent OFET measurements. In contrast, the microwave mobility of DHPT-SC exhibits a stronger temperature dependence and the activation energy is similar to the results obtained for the OFET measurements upon cooling. The lower activation energy for DHBTP-SC suggests that the structural order in this material is higher than that in DHPT-SC, at least on a local scale, which is consistent with the higher microwave mobility at room temperature. This higher structural order is also supported by the fact that absorption spectrum of DHPT-SC is rather featureless, whereas that of DHBTP-SC exhibits a weak vibronic progression. Also, our AFM studies on DHBTP-SC layers revealed the growth of large crystallites upon prolonged annealing, again indicating the ability of the molecules to form highly ordered domains.

If the intrinsic (TRMC) mobility for DHBTP-SC is higher because of a higher degree of ordering, it seems likely that the reversed trend of the mobility values obtained from transistor measurements is due to inefficient transport between grains. In the cruciform DHBTP-SC, highly ordered domains are formed with a high intrinsic mobility but with relatively inefficient charge transport between different domains. In DHPT-SC, a more homogeneous structure is formed with a lower degree of order inside the grains, but with higher charge-transport efficiency between grains. This leads to an overall higher mobility in the transistor measurement and similar activation energies in the OFET and PR-TRMC measurements. It suggests that the charge transport between order domains rather than the transport within the crystallites is the most important process determining the transistor mobility.

This conclusion is in agreement with recent studies on P3HT with different molecular weights ($M_w \approx 3000-35\,000$ g/mol).[5a,d] Here, we found that field-effect mobility decreases significantly with lowering molecular weight. This fact was attributed to the smaller degree of crystallinity in the low-M_w fraction as determined from the DSC result measured in powder. Although the XRD results confirmed that highly ordered crystallites were found within this fraction, the overall mobility was determined by the slow charge-carrier transport within the amorphous region. On the contrary, the high-M_w fraction exhibited a higher degree of crystallinity but smaller crystallites with diameter smaller than the chain length; therefore, the polymer chain will most likely interconnect the neighboring domains.

Investigations by McGehee and co-workers suggested that the low mobility of the short chain sample might also originate from the misalignment of crystalline domains at the semiconductor interface.[5b] In fact, using a liquid crystalline semiconductor that can be homogeneously aligned might improve the efficiency of the intergrain transport.

3. Conclusions

In conclusion, thiophene-based swivel cruciforms are shown to form highly crystalline layers with field-effect mobilities up to 0.012 cm^2/Vs. Films of DHPT-SC appeared to be morphological stable upon annealing, whereas thermal treatment of the phenyl containing cruciform DHBTP-SC resulted in the growth of large crystallites. For both swivel cruciforms, the field-effect mobility was found to be temperature activated, with an activation energy of ca. 80−90 meV upon heating and ca. 50 meV upon cooling. Interestingly, PR-TRMC measurements on the phenyl-containing cruciform yielded a very weak temperature dependence of the microwave mobility. Compared to the mobility measurements in the OFET, PR-TRMC measures the transport of charges inside single grains of the material and the trapping at grain boundaries is insignificant. This result suggests a high structural order of this material on the microsopic level. We conclude that the electrical properties of these layers on macroscopic scales are ultimately determined by charge transport between crystalline domains.

4. Experimental Section

Thin-Film Preparation. For the absorption and photoluminescence measurements of the thin films, DHBTP-SC and DHPT-SC were dissolved into the chloroform (10 mg/mL) and spun with a speed of 1500 rpm onto the glass substrates. For the XRD, AFM, and OFET measurements, prior to deposition of the oligomers, the surface of the Si/SiO_2 substrates were carefully cleaned with several common solvents, activated with oxygen plasma, and treated with hexamethyldisilazane (HMDS) for 26 h at 60 °C.[16a] The solutions of oligomers were then spun onto those treated substrates. The overall thicknesses of the thin films are in the range of 40−55 nm. In fact, we have used the same substrates for the AFM and OFET measurements.

Instrumentation. Oligomer DHBTP-SC and DHPT-SC were easily dissolved in chloroform at room temperature. Optical absorption spectra were measured with a Perkin-Elmer Lambda 19 UV−vis spectrometer. Photoluminescence emission spectra were recorded by using a Perkin-Elmer LS 55 Luminescence spectrometer. Differential scanning calorimetry (DSC) thermograms were measured using a Perkin-Elmer Thermal Analysis DCS-7 calibrated with Indium (99.99% pure). The measurements were carried out under an argon atmosphere with heating and cooling rates of 10 °C/min. Melting and crystallization temperatures were determined by taking the peak values of the heating and cooling scans, respectively.

Atomic force microscopy (AFM) equipment from Digital Instruments Nanoscope IIIa working in the tapping mode was used to investigate the morphologies of the dry thin films on top of Si/SiO_2 substrates. Measurements were done at room temperature in

air with a relative humidity of 30−40%. Height and phase images were recorded with scan rates of 2−4 lines/s and a resolution of 512 pixels × 512 pixels using microfabricated silicon nanoprobes (length = 125 μm and width = 30 μm) with a spring constant between 17 and 64 N m^{-1}.

X-ray diffraction of the thin films was carried out to investigate the crystallinity and the packing of the molecules. We have measured the thin films of both oligomers using coplanar X-ray diffraction (XRD) techniques at a home diffractometer equipped with a Goebel-mirror. The 2θ scans were carried out at different incidence angles with respect to the sample surface, below or above the critical angle of total reflection, α_c; the penetration depth of the X-ray beam into the sample was controlled in this way.

Field-effect transistors were fabricated from oligomer DHBTP-SC and DHPT-SC using bottom gate geometry on highly doped *n*-type silicon wafers, acting as the gate electrode. A thermally grown 300 nm thick silicon dioxide layer with a capacitance of 11 nF/cm^2 served as the gate insulator. The source and drain electrodes with interdigitating structure from Au (thickness = 100 nm) were evaporated on top of the thin films (channel length 100 μm and total channel width 148.5 mm). Annealing was done prior to the deposition of the source and drain electrodes. Output and transfer characteristics with the scan rate of 2.5 and 2 points/s were measured using the Agilent 4155C semiconductor parameter analyzer from Hewlett-Packard. OFET temperature-dependent measurements were measured by heating the OFET devices in situ using a DCT 600 thermal controller from Digit Concept S. A. (Brussels, Belgium), and nitrogen gas was used for cooling the sample. For each oligomer, it took ca. 45 min for each temperature scan (heating from RT to 120 °C or vice versa for the cooling) and ca. 100 min for the whole cycles. All preparation processes and the characterization of the devices were performed inside a N_2-filled glove box.

Pulse-radiolysis time-resolved microwave vonductivity (PR-TRMC) measurements were carried out at the Delft University of Technology (DelftChemTech), The Netherlands. The PR-TRMC technique and methods of data analysis have been described in detail in other publications;[20] therefore, only a brief description is given in here. Approximately 30 mg of the powder of oligomers DHBTP-SC and DHPT-SC were compressed into a perspex sample holder and placed in a Q-band microwave cell. The samples were irradiated with a single (0.3−50 ns duration) pulse of 3 MeV electrons from Van de Graaff accelerator. This leads initially to a uniform distribution of positive and negative charges in the samples. The change in conductivity induced by the generation of charge carriers is measured by monitoring the decrease in microwave power reflected by the cell upon irradiation. The fractional change in the reflected microwave power is directly proportional to the change in conductivity, $\Delta\sigma$. Temperature dependence was measured upon heating; we also measured a few temperatures on cooling but no noticeable difference was observed. Measurements for both compounds were performed on the same day, and the system was allowed to stabilize approximately 15−20 min at each temperature before measuring. The microwave frequency range was between 27 and 38 GHz, and the maximum electric field strength within the sample was ca. 10 V/m. If the concentration of charge carriers generated by irradiation is known, the measured conductivity can be used to calculate the charge-carrier mobility. In this work, we used a relation by Allig that relates the initial yield of charge carriers to the band gap of the material studied.[20] The initially generated charges can decay during the pulse by recombination or trapping. Therefore, taking the estimated initial yield gives an upper limit to the concentration of charge carriers in the materials and leads to a lower limit of the charge-carrier mobility (μ_{min}). Additionally, in PR-TRMC experiments both positive and negative charge carriers are created, both of which can contribute to the conductivity signal. Hence, the PR-TRMC mobility values represent the sum of the positive and negative charge carriers.

Synthesis. *2,5-di-(5-hexylbithienyl)-1-chlorobenzene (HTP):* A solution of 5-(4,4,5,5-tetramethyl-1,3,2-dioxoborolan-2yl)-5′-*N*-hexyl-2,2′-bithienyl (3 g, 8 mmol) in dry THF (50 mL) was added slowly to a mixture of 1,4-dibromo-2-chlorobenzene (0.85 g, 3.14 mmol), K_2CO_3 (0.87 g, 6.3 mmol), and tetrakis(triphenylphosphino)-palladium(0) (0.15 g, 0.13 mmol) in dry THF (200 mL) at reflux and subsequently stirred for a further 24 h under reflux with the exclusion of light. The reaction mixture was then diluted with chloroform and washed with water, saturated aqueous EDTA solution, and brine. The organic phase was dried over $MgSO_4$, and the solvent was removed by rotary evaporation. The residue was purified by column chromatography on silica gel using a toluene/hexane mixture (1:9) as the eluent. The solvent was once again removed, and the residue was recrystallized from *n*-heptane to afford HTP as a yellow powder in a yield of 67%.

^{1}H NMR (400 MHz, $C_2D_2Cl_4$): δ 7.61 (d, 1H, J = 1.8 Hz), 7.49 (d, 1H), 7.41 (dd, 1H, J = 1.9 Hz, J = 8.2 Hz), 7.28 (d, 1H, J = 3.9 Hz), 7.18 (d, 1H, J = 3.8 Hz), 7.03 (dd, 2H, J = 3.9 Hz, J = 10.1 Hz), 6.97 (t, 2H, J = 3.8 Hz), 6.65 (d, 2H, J = 3.5 Hz), 2.73 (t, 4H, J = 7.6 Hz), 1.62 (m, 4H), 1.28 (m, 12H), 0.82 (td, 6H, J = 5.0 Hz, J = 6.8 Hz). ^{13}C NMR (100 MHz, $C_2D_2Cl_4$): δ 146.4, 146.3, 140.0, 139.1, 138.6, 138.0, 134.6, 134.5, 132.5, 131.5, 131.3, 128.8, 127.4, 125.3, 125.2, 125.1, 124.3, 124.2, 124.1, 124.0, 123.4, 31.9, 31.8, 30.5, 29.1, 22.9, 14.5. MS (FD, 70 eV): m/z = 609 (M^+). Anal. Calcd for $C_{34}H_{37}ClS_4$: C, 67.01; H, 6.12; S, 21.05. Found: C, 66.88; H, 5.94; S, 21.13.

2,2′,5,5′-Tetrakis-(ω-hexylbithienyl)-1,1′-biphenyl (DHBTP−SC): $Ni(COD)_2$ (0.41 g, 1.5 mmol), bipyridyl (0.23 g, 1.5 mmol), and HTP (0.6 g, 1 mmol) were dissolved in dry THF (20 mL). Cyclooctadiene (0.17 g, 1.6 mmol) was added to the solution, and the reaction mixture was stirred at 80 °C for 48 h. The mixture was subsequently diluted with chloroform and washed with brine, saturated aqueous EDTA solution, and once again with brine. The organic phase was dried over $MgSO_4$, and the solvent was removed by rotary evaporation. The residue was purified via column chromatography with silica gel using a toluene/hexane mixture (95:5) as eluent and was recrystallized from ethanol to give DHBTP-SC in 25% yield.

^{1}H NMR (400 MHz, $C_2D_2Cl_4$): δ 7.58 (qd, 4H, J = 1.9 Hz, J = 3.8 Hz), 7.48 (d, 2H, J = 8.7 Hz), 7.22 (d, 2H, J = 3.8 Hz), 7.03 (d, 2H, J = 3.7 Hz), 6.97 (d, 2H, J = 3.5 Hz), 6.76 (dd, 4H, J = 3.6 Hz, J = 10.6 Hz), 6.65 (d, 2H, J = 3.5 Hz), 6.54 (d, 2H, J = 3.6 Hz), 6.37 (d, 2H, J = 3.6 Hz), 2.73 (td, 8H, J = 7.5 Hz, J = 20.1 Hz), 1.64 (m, 8H), 1.30 (m, 24H), 0.86 (q, 12H, J = 6.9 Hz). ^{13}C NMR (100 MHz, $C_2D_2Cl_4$): δ 146.2, 145.7, 141.6, 140.5, 139.6, 138.5, 138.0, 134.9, 134.7, 133.5, 133.0, 130.2, 127.4, 125.3, 125.0, 124.8, 124.6, 124.3, 123.9, 123.7, 123.6, 123.5, 31.8, 30.5, 30.4, 30.0, 29.9, 29.1, 29.0, 22.9, 14.5, 14.4. MS (FD, 70 eV): m/z = 1148.5 (M^+). Anal. Calcd for $C_{68}H_{74}S_8$: C, 71.15; H, 6.50; S, 22.35. Found: C, 71.44; H, 7.06; S, 22.54.

Acknowledgment. This work was financially supported by the DFG under project SP1121, the *F*ond der Chemischen Industrie, and the Ministerium für Wissenschaft, Forschung and Kultur of Brandenburg.

Supporting Information Available: AFM images of DHBTP-SC and DHPT-SC recorded for as-prepared and annealed at 120 °C

(20) Warman, J. M.; de Haas, M. P.; Dicker, G.; Grozema, F. C.; Piris, J.; Debije, M. G. *Chem. Mater.* **2004**, *16*, 4600.

for different time periods, ^{1}H NMR spectra of HTP and DHBTP-SC in $C_2D_2Cl_4$, ^{1}H−^{1}H COSYLR of HTP in $C_2D_2Cl_4$, ^{1}H−^{1}H COSY of DHBTP-SC in $C_2D_2Cl_4$, ^{1}H−^{1}H COSYLR of DHBTP-SC in $C_2D_2Cl_4$, ^{13}C NMR spectra of DHBTP-SC in $C_2D_2Cl_4$, ^{13}C NMR spectrum of the aromatic region of DHBTP-SC in $C_2D_2Cl_4$, ^{13}C NMR spectrum of the alkyl region of DHBTP-SC in $C_2D_2Cl_4$. This material is available free of charge via the Internet at http://pubs.acs.org.

CM062000P